

CONSTRAINTS ON THE SIZE EVOLUTION OF BRIGHTEST CLUSTER GALAXIES¹

AMY E. NELSON

Board of Astronomy and Astrophysics, University of California, Santa Cruz, CA, 95064, E-Mail:
anelson@ucolick.org

LUC SIMARD², DENNIS ZARITSKY

Steward Observatory, 933 N. Cherry Ave., University of Arizona, Tucson, AZ, 85721, E-Mail: lsimard,
dzaritsky@as.arizona.edu

JULIANNE J. DALCANTON

Box 351580, University of Washington, Seattle, WA, 98195, E-Mail: jd@toast.astro.washington.edu
AND

ANTHONY H. GONZALEZ

Harvard-Smithsonian Center for Astrophysics, 60 Garden Street, Cambridge, MA, 02138, E-Mail:
anthony@head-cfa.harvard.edu

Astrophysical Journal Accepted, 22 October 2001

ABSTRACT

We measure the luminosity profiles of 16 brightest cluster galaxies (BCGs) at $0.4 < z < 0.8$ using high resolution F160W NICMOS and F814W WFPC2 HST imaging. The heterogeneous sample is drawn from a variety of surveys: seven from clusters in the Einstein Medium Sensitivity Survey (EMSS; Gioia & Luppino 1994), five from the Las Campanas Distant Cluster Survey and its northern hemisphere precursor (LCDCS; Dalcanton et al. 1997; Gonzalez et al. 2001; Nelson et al. 2001a), and the remaining four from traditional optical surveys (Spinrad 1980; Koo 1981; Gunn et al. 1986; Couch et al. 1991). We find that the surface brightness profiles of all but three of these BCGs are well described by a standard de Vaucouleurs ($r^{1/4}$) profile out to at least $\sim 2r_e$ and that the biweight-estimated NICMOS effective radius of our high redshift BCGs ($r_e = 8.3 \pm 1.4$ kpc for $H_0 = 80$ km s⁻¹ Mpc⁻¹, $\Omega_m = 0.2$, $\Omega_\Lambda = 0.0$) is ~ 2 times smaller than that measured for a local BCG sample (Graham et al. 1996). If high redshift BCGs are in dynamical equilibrium and satisfy the same scaling relations as low redshift ones, this change in size would correspond to a mass growth of a factor of 2 since $z \sim 0.5$. However, the biweight-estimated WFPC2 effective radius of our sample is 18 ± 5.1 kpc, which is fully consistent with the local sample. While we can rule out mass accretion rates higher than a factor of 2 in our sample, the discrepancy between our NICMOS and WFPC2 results, which after various tests we describe appears to be physical, does not yet allow us to place strong constraints on accretion rates below that level.

Subject headings: galaxies: clusters: general — galaxies: evolution — galaxies: formation — galaxies: elliptical

1. INTRODUCTION

Brightest cluster galaxies (BCGs) have been studied, both photometrically and spectroscopically, in great detail at low redshift because of their unique characteristics and location (e.g., Hoessel et al. 1980; Schombert 1986; Postman & Lauer 1995). BCGs are the most massive and luminous galaxies in the universe, with central velocity dispersions $\sigma \sim 300\text{--}400$ km s⁻¹ (Dressler 1979; Carter 1985; Fisher et al. 1995), and typical luminosities $\sim 10 L_*$, where $L_* = 1.0 \times 10^{10} h^2 L_\odot$, (Sandage & Hardy 1973; Hoessel et al. 1980; Schombert 1986). Rather than simply being “the brightest of the bright,” BCGs are drawn from a different luminosity function (Dressler 1978) and follow tighter scaling relations, for example the $r_e - \mu_e$ relation (Hoessel et al. 1987), than other cluster ellipticals. Their remarkably homogeneous luminosity, $\sigma_V \simeq 0.35$ mag, ($\sigma_V \simeq 0.30$ mag when applying corrections based upon environment; e.g., Sandage & Hardy 1973; Hoessel et al. 1980), suggests they may experience a unique evolutionary history. Because BCGs are typically located near the center of the cluster

potential, they may preferentially accrete material from tidally stripped cluster galaxies (Richstone 1976) or merge with other cluster members (Ostriker & Hausmann 1977). Observed correlations between BCG structural parameters and luminosity (such as the luminosity-shape relation of Hoessel et al. 1980) may be signs of such accretion events (Ostriker & Tremaine 1975; Schneider et al. 1983).

Studies comparing the luminosity of high redshift BCGs to their low redshift counterparts find indirect evidence of mass accretion in BCGs since $z \sim 1$ (Aragon-Salamanca et al. 1998, hereafter ABK98; Burke et al. 2000; Nelson et al. 2001a). The amount of inferred evolution, however, is tied to environment. BCGs in clusters with low x-ray luminosity ($L_x < 2.3 \times 10^{44}$ ergs s⁻¹) fade less with decreasing redshift than expected from the aging of their stellar populations (ABK98; Burke et al. 2000; Nelson et al. 2001a). The proposed explanation for this observation is that these galaxies are accreting roughly enough mass in stars to counter the expected passive evolution – about a factor of 2 to 4 increase in mass since $z \sim 1$ (ABK98). On the other hand, the luminosities of high L_x BCGs do

¹ Based on observations made with the NASA/ESA *Hubble Space Telescope* which is operated by AURA, Inc., under contract with NASA.

² Guest User, Canadian Astronomy Data Center, which is operated by the National Research Council of Canada, Herzberg Institute of Astrophysics, Dominion Astrophysical Observatory.

match the predictions of passive evolution models (Burke et al. 2000; Nelson et al. 2001a), which limits the possible amount of mass these BCGs accrete to less than a factor of 2.

Unfortunately, the inferred mass accretion rates rely on the assumption that increases in luminosity are attributable to increases in mass. A way to test the hypothesis of accretion in BCGs is to measure the structural parameters of the BCGs (mass, size, velocity dispersion, surface brightness). Locally, BCGs conform to the fundamental plane relations between $\log r_e - \log \sigma - \langle \mu \rangle$ derived by Dressler (1987) for lower luminosity ellipticals (Oegerle & Hoessel 1991). Because they lie on the fundamental plane, the local BCGs appear to be in dynamical equilibrium and changes in mass should produce corresponding changes in size. If we presume that high redshift BCGs also satisfy these scaling relations on the grounds that high redshift ellipticals are observed to lie on the fundamental plane (Kelson et al. 1997), then a comparison of the sizes of local and distant BCGs should help constrain accretion models. Alternatively, highly irregular BCG luminosity profiles would argue that these galaxies are not in dynamical equilibrium. The major obstacle for such a study is that measuring structural parameters of high redshift BCGs requires high angular resolution imaging.

We present the first study of the structural parameters of high redshift BCGs using *Hubble Space Telescope* NICMOS F160W and WFPC2 F814W imaging and search for direct signatures of accretion events in these galaxies. The use of infrared data is important because, even for our most distant clusters, these wavelengths probe the older, more quiescent stellar populations, thereby making comparisons to local samples more direct. Without prior knowledge, a homogeneous data set that minimizes one’s sensitivity to potential recent star formation is necessary for this study. If the high-redshift BCGs are found to be quiescent, relaxed systems, then one might, with caution, further explore the WFPC2 archive to enlarge the sample. In §2 we describe our heterogeneous sample of 16 BCGs at $0.4 < z < 0.8$ and the HST data. In §3, we describe the three different methods we use to measure BCG effective radii including GIM2D, a package which we utilize to fit the surface brightness profiles of the BCGs. In §4, we present the best fitting models to the surface brightness profiles and investigate the mass accretion rate of BCGs since $z \sim 0.5$. Finally, we summarize our conclusions in §5.

2. THE DATA

2.1. *HST*/NICMOS

The 16 BCGs we analyze are a heterogeneous sample culled from several sources – seven from clusters in the Einstein Medium Sensitivity Survey (EMSS; Gioia & Luppino 1994), five from the Las Campanas Distant Cluster Survey and its northern hemisphere precursor (LCDCS; Dalcanton et al. 1997; Gonzalez et al. 2001; Nelson et al. 2001a), and the remaining four from traditional optical surveys (Spinrad 1980; Koo 1981; Gunn et al. 1986; Couch et al. 1991). The BCGs were observed by the *Hubble Space Telescope* with the NICMOS camera and F160W filter from June 1997 through March 1998 in the “snapshot” mode as part of program GO 7327 (PI: Dalcanton).

The images were obtained using the NIC2 camera configuration ($19'2 \times 19'2$ field of view, $0.075'' \text{ pixel}^{-1}$) in MULTIACCUM mode with NSAMP=16. Observations consist of three dithered exposures per object with exposure times of 256 seconds per dither position for BCGs at $z < 0.6$ and 352 seconds per dither position for BCGs at $z > 0.6$. The NIC2 image datasets are listed in Table 1. NICMOS images calibrated “on-the-fly” from the HST data archive are generally of inferior quality because the automated reduction pipeline, CALNICA, does not correct for non-linear bias levels and time-varying changes in the dark current level (the so-called “pedestal effect”). Therefore, we calibrate the raw science images using the NICPIPE routine available in the STSDAS Version 2.2 IRAF package. This pipeline incorporates the standard reduction procedure of CALNICA, but in addition uses the tasks BIASEQ and PEDSUB to correct for non-linear bias level drift and quadrant-dependent residual bias level.

We calculate F160W magnitudes (denoted $H_{160,AB}$ hereafter) in Oke’s AB system (Oke & Gunn 1983) according to the following expression:

$$H_{160,AB} = -2.5 \log(PHOTFNU \times CR) + 8.9, \quad (1)$$

where CR is the count rate and $PHOTFNU$ is the *HST* photometric conversion between countrates and fluxes in units of Jy s DN^{-1} in the image headers. Galaxy magnitudes are corrected for extinction using the dust IR emission maps of Schlegel et al. (1998) but are not K-corrected.

The galaxy identified as the BCG was generally not known prior to this program. Because the field of view of the NICMOS images is small, we do not simply choose the brightest galaxy on the image as the BCG. Instead, we identify the BCGs on large optical and/or near-IR images for all but two clusters – MS0302.5+1717 and MS1333.3+1725 (Gioia & Luppino 1994). For the LCDCS clusters, the BCG is defined as the galaxy with the brightest total *I*-band magnitude located within $350h^{-1}$ kpc of the cluster center. To reduce contamination by bright blue foreground galaxies, we exclude BCG candidates whose colors are 0.4 mag bluer than the location of the red envelope in the cluster color-magnitude diagram (see Nelson et al. 2001a for details). 1100+4620 does not have *I*-band imaging and therefore the BCG is determined using ground-based *Kp* imaging. We identify the BCGs in CL0016+16, J1888.16CL, CL0317+1521, and CL1322+3027 using the cluster contour plots and *K*-band photometry files published by Aragon-Salamanca et al. (1993). Five of the seven EMSS BCGs are selected using various optical images and identifications published in the literature (Luppino & Gioia 1992; Clowe 1998; Luppino & Gioia 1999; Clowe et al. 2000). Finally, we could not find BCG identifications in the literature for the remaining two EMSS clusters (MS0302.5+1717 and MS1333.3+1725). The NICMOS images for both of these clusters contain a large, dominant galaxy in the field of view which we define to be the BCG. We caution, however, that the BCG identifications for these two clusters are less certain.

2.2. *HST*/WFPC2

We also make use of archival *HST*/WFPC2 images taken in the F814W filter available for 9 BCG’s in our NIC-

MOS sample. The datasets are listed with their exposure times in Table 1. These archival images were recalibrated “on-the-fly” through the Canadian Astronomy Data Center (CADC) standard pipeline. WFPC2 images covers a larger field of view ($36''.8 \times 36''.8$ for the Planetary Camera and $80'' \times 80''$ for each of the three Wide-Field Camera detectors) than NIC2. At $z = 0.6$, the F814W filter samples the rest-frame wavelength range 4578–5676 Å. As a comparison, the NIC2 F160W filter at that redshift samples the rest-frame wavelength range 8750–11250 Å.

3. ANALYSIS

One of the main problems in measuring the sizes of high-redshift brightest cluster galaxies are the systematic errors in the measurement of the sky. This problem is exacerbated by the fact that some BCGs locally exhibit steep (Sérsic index $n > 4$) profiles and a significant amount of flux in their broad outer wings (Graham et al. 1996). Sky errors are of particular concern for the NIC2 detector because it covers a relatively small sky area, which can lead to contamination of flat-fielding and sky subtraction. Because of the uncertainties involved in the sky determination, we decided to measure BCG sizes in three different ways: curve of growth with circular apertures (Section 3.1), Point-Spread-Function (PSF)-convolved surface brightness models (Section 3.2), and isophotal ellipse fitting (Section 3.3).

3.1. Curve of Growth

For each BCG in our sample, we measure NIC2 and WFPC2 circular half-light radii by computing the galaxy flux within concentric apertures and interpolating this curve of growth to find the radius that contains half of the total flux given by the asymptotic flux value at large radii. The curves of growth were measured directly from the images and not from surface brightness models such as the ones obtained in Section 3.2. Typical maximum radii for the NIC2 and WFPC2 curves of growth are 6.8–9.0 arcseconds (90–120 pixels) and 20 arcseconds (200 pixels) respectively. The sky background is manually adjusted until the integrated flux is asymptotically flat over a range of at least 30 pixels. Flux from neighboring galaxies is carefully excluded from the curves of growth using segmentation images produced with the SExtractor galaxy photometry package (Bertin & Arnouts 1996). The actual BCG flux in each excluded pixel, which would have been included in the curve of growth in the absence of neighbors, is calculated using its symmetric counterpart about the center of the BCG. The NIC2 curve-of-growth BCG half-light radii (in arcseconds and in kpc) is presented in Table 2 (Columns 3 and 4). We list three values for each BCG because a different curve of growth was obtained independently for each of the three NIC2 dither positions. The typical variations in half-light radii from one dither position to another are $\sim 0''.1$ – $0''.2$. The WFPC2 curve-of-growth half-light radii are presented in Table 3.

3.2. BCG Surface Brightness Profile Fitting

The BCG surface brightness profiles are fit using the GIM2D package, which is designed to perform 2D disk+bulge deconvolutions of low signal-to-noise images of distant galaxies (Simard 1998; Simard et al. 2001).

The GIM2D bulge component profile is a Sérsic profile (Sérsic 1968) of the form:

$$\Sigma(r) = \Sigma_e \exp\{-b[(r/r_e)^{1/n} - 1]\}, \quad (2)$$

where $\Sigma(r)$ is the surface brightness along the semimajor axis at radius r , r_e is the semi-major axis effective radius, and Σ_e is the effective surface brightness. The parameter b is set equal to $1.9992n - 0.3271$ to ensure that r_e is the projected radius enclosing half of the light. A standard de Vaucouleurs profile is obtained by setting $n = 4$. The flux interior to the radius r is given by

$$F(r) = 2\pi n \Sigma_e r_e^2 \frac{e^b}{b^{2n}} \gamma(2n, b), \quad (3)$$

where $\gamma(2n, x)$ is the incomplete Gamma function with $x = b(r/r_e)^{1/n}$. Equations 2 and 3 are given in their circularly symmetric form for the sake of simplicity, but GIM2D does consider the intrinsic (i.e. before PSF convolution) ellipticity of the bulge by including bulge ellipticity e and position angle ϕ_b as additional parameters.

The GIM2D disk component is a simple exponential profile of the form:

$$\Sigma(r) = \Sigma_0 \exp(-r/r_d). \quad (4)$$

Σ_0 is the face-on central surface brightness, and r_d is the semi-major axis exponential disk scale length. The disk is assumed to be infinitely thin. The total flux in the disk is given by:

$$F_{\text{disk}} = 2\pi r_d^2 \Sigma_0. \quad (5)$$

The projected surface brightness distribution of the disk inclined at any angle i is calculated by integrating Equation 4 over the area in the face-on disk plane seen by each projected pixel. The position angle ϕ_d of the disk is also a fitting parameter.

Mosaicing dithered images with non-integer pixel shifts requires flux interpolation between pixels and corrections for geometric distortion. For undersampled HST images such as ours, these processes severely distort the shape of the PSF and destroy the uncorrelated noise characteristics of the original images. To circumvent these potential difficulties, GIM2D allows for fitting multiple, dithered individual images simultaneously. We use this mode for the NIC2 data. The WFPC2 images are also undersampled, but because our archival images have integer pixel shifts they are combined without information loss, and the combined image is analyzed with GIM2D.

HST point-spread-functions vary spatially across the image, and additionally NICMOS PSFs vary temporally. A PSF must therefore be individually generated for each object of interest. We use the software package TINYTIM V5.0c (Krist 1993) to generate PSFs that include both types of variation for each BCG position and observation date (for NIC2). Our NIC2 PSFs are $1''.9 \times 1''.9$, and our WFPC2 PSFs are $2''.4 \times 2''.4$. Both types of PSFs are oversampled by a factor of 5. To compare directly to undersampled HST data, GIM2D creates a surface brightness model on an oversampled grid, convolves it with the corresponding oversampled PSF, shifts it to a subpixel position specified by the values of the fitting parameter dx

and dy and rebins the resulting profile to the detector’s resolution.

We use SExtractor segmentation images to isolate the BCGs from their neighbors. As SExtractor performs source detection, it deblends sources using flux multi-thresholding (Bertin & Arnouts 1996). The result of deblending are segmentation images in which pixels belonging to the same object are all assigned the same flag value, and sky background pixels are flagged by zeroes. GIM2D fits are performed on all pixels flagged as the target object *or* background in the SExtractor segmentation images. The rationale behind not just fitting “object” pixels is that considering only the pixels interior to the boundary between object and sky, which is sharply delineated by the isophote corresponding to the detection threshold, would exclude information contained in the pixels below that threshold.

We fit the NIC2 BCG images with pure de Vaucouleurs ($n = 4$) bulge and full de Vaucouleurs bulge + exponential disk models. Although the sky level can be a free parameter in GIM2D, we fix the sky level to the value determined from the curve of growth analysis of Section 3.1 because of the relatively large angular extent of the galaxies and the non-uniformity of the background. The results from the GIM2D NIC2 fits are shown in Table 2. The GIM2D half-light radii are measured along the semi-major axis (SMA) of the BCG. SMA radii can be converted to “circular” radii according to $r_{circ} = r_{sma} \sqrt{1 - e_{bcg}}$ where e_{bcg} is the ellipticity of the BCG. We list both SMA and circular radii in Table 2. Residual images are visually inspected to determine which model (pure bulge or bulge+disk) yields a better fit. The better model is listed in Column 13 (“PB” = Pure Bulge, “BD” = Bulge+Disk and “EQ” = Equally Good) of Table 2. Although seven BCGs are fit better by a bulge+disk model, this result does *not* imply that actual disks are present in those BCGs. The residual images suggest that an intrinsic change in ellipticity (i.e. over what one would expect from pure PSF smoothing) and position angle as a function of radius may be responsible for the preference of a bulge+disk model.

We fit the deeper and larger WFPC2 images with three different models: a pure de Vaucouleurs bulge, a de Vaucouleurs bulge + exponential disk and a pure Sérsic of parameter n . We allow n to vary between 1 and 6. Two sets of fits are performed: one with the sky fixed to the value obtained from the curve of growth analysis and one with the sky left as a free parameter. The results are shown in Table 3. There are two lines per BCG in Table 3. The first and second lines give the results of the fixed and floating background fits respectively. The half-light radius of the best model, as determined through visual inspection of the residual images, is underlined for each BCG. The advantage of using so many different models is the ability to see the systematic effects on the measurement of the BCG half-light radii introduced by the choice of a particular model. The significant disagreements between models arises because the half-light radius depends on the measured total flux, which depends on the details of the poorly constrained outer regions of the galaxy. Table 3 lists six radii for each BCG, and the variations among these six values reflect errors due to the modeling of the sky and the flux in the outer wings of the galaxy.

3.3. Elliptical Isophote Fitting

Elliptical isophote fitting provides yet another way to measure BCG sizes and to demonstrate how bulge+disk model fits can introduce a disk component to model a pure elliptical galaxy with ellipticity and position angle radial variations. We use the task ELLIPSE in the IRAF/STSDAS/ISOPHOTE package to fit isophotal ellipses to the WFPC2 images of seven out of nine BCGs. We could not acceptably fit MS1621 and MS0451. The “BCG” in MS1621 is actually a close pair of early-type looking galaxies, and the MS0451 BCG is adjacent to another large galaxy.

In this fitting, we allow the isophote center, ellipticity, and position angle to vary with radius. In contrast, introducing radial variations is not practical in model fitting because of the large number of degrees of freedom. For example, the GIM2D model has one center, one ellipticity and one position angle per component (bulge or disk). The isophotal ellipse fitting results are presented in Table 4. The Table presents the difference in ellipticity between the outer and inner isophotes, $\Delta e(\text{ISO})$, the difference in ellipticity between the outer (disk) component and the inner (bulge) component, $\Delta e(\text{GIM2D})$, the difference in isophote position angle between the outer and inner isophotes, $\Delta \phi(\text{ISO})$, the position angle difference between the disk and bulge components, $\Delta \phi(\text{GIM2D})$, and the pixel shifts in the isophote center between the outer and inner isophotes, Δx and Δy . The close correlations between $\Delta e(\text{ISO})$ and $\Delta e(\text{GIM2D})$ and between $\Delta \phi(\text{ISO})$ and $\Delta \phi(\text{GIM2D})$ suggest that bulge+disk models fit some of the BCG profiles better than bulge-only models because the extra freedom in the two component models is being used to fit the radial variations in the ellipticity and position angle.

3.4. NIC2 Curve-of-Growth Simulations

To test how well we recover true half-light radii from NIC2 curves of growth, we perform a set of simulations. We choose five BCGs with both NIC2 and WFPC2 images: MS1137, CL1322, MS2053 and CL0016. We create three types of NIC2 simulations for each BCG. For the first simulation, we take the NIC2 best-fit pure $r^{1/4}$ GIM2D model image, and we insert it in another location on the NIC2 image. This type of simulations is labeled as “NIC2 $r^{1/4}$ ” in Table 5. For the second simulation (labeled as “NIC2 B+D” in Table 5), we take the NIC2 best-fit bulge+disk GIM2D model, and we insert it in another location on the NIC2. For the third simulation (labeled as “WFPC2 $r^{1/4}$ ” in Table 5), we use the half-light radius of the best-fit WFPC2 model to create a pure $r^{1/4}$ model. We normalize this model to have the measured flux, and we insert it in the NIC2 image. We analyze all three types of simulations using the same curve-of-growth procedure that we use to measure circular half-light radii from the real data. See Table 5 for the results. No model fits are involved. We compare the radii recovered from the curve-of-growth to the circular input values. F_r is the ratio of the recovered and input radii, and F_f is the ratio of the recovered and input total fluxes. Using the results from all three types of simulations, we find that the NIC2 half-light radius is systematically underestimated by a mean of 20%. The cause of the problem is not simply the lack of sky in the

NIC2 images because one of the galaxies with the largest WFPC2 half-light radii (MS1137) is recovered well.

4. DISCUSSION

4.1. Are High-Redshift BCGs in Dynamical Equilibrium?

The presence of significant distortions indicating recent major mergers and/or an ellipticity distribution that is significantly different from the local BCG population would be clear morphological signs that high-redshift BCGs are not in dynamical equilibrium. However, the surface brightness profiles of our 16 BCGs are quite regular (Figure 1). To generate the plotted profiles, we fit elliptical isophotes to the data using the IRAF task ELLIPSE. We use the best fitting model galaxy parameters listed in Table 1 to compute the slope and zero-point of the corresponding PSF-deconvolved de Vaucouleurs profile. The semi-major axis radii are converted from arcsec to kpc assuming $H_0 = 80 \text{ km s}^{-1} \text{ Mpc}^{-1}$, $\Omega_m = 0.2$, and $\Omega_\Lambda = 0.0$. The BCG surface brightnesses have been corrected for cosmological $(1+z)^4$ dimming, but are not K -corrected (K -corrections for an elliptical galaxy in the H -band are typically ~ 0.2 - 0.4 mag for this redshift range). Figure 1 demonstrates that all but three of our BCGs are well described by a de Vaucouleurs profile beyond the resolution limit and out to at least ~ 2 NIC2 r_e . The notable exceptions are MS0302.5+1717, CL0016, and 1041+4626. The BCG MS0302.5+1717 is actually best-fit by a pure exponential disk profile. We note, however, that this BCG is selected directly from the NICMOS images and therefore its identification is less certain. The BCG CL0016 has a prominent dust lane, and the BCG 1041+4626 lies at the corner of a frame where the local background varies significantly. Additionally, we search for azimuthal asymmetry in the BCG profiles by subtracting the best fitting 2D galaxy model from the data. With the exception of the BCG in MS0302.5+1717, which is not well fit by an $R^{1/4}$ profile, and the BCG in CL0016, which shows a dust lane, we find that the BCG images do not have significant 2-dimensional residuals (the best fitting models typically yield $\chi^2 \sim 1$). Consistent with this finding, our high redshift BCGs have similar ellipticities ($0.0 < \epsilon < 0.5$) to their local counterparts (Graham et al. 1996). We conclude that the BCGs exhibit no signs of being far from dynamical equilibrium.

4.2. Comparison with Local BCG Sizes

The good agreement between our BCG surface brightness profiles and a standard de Vaucouleurs profile in conjunction with the lack of any significant 2-dimensional residuals argues against recent major accretion events. However, cumulative minor merger events over time may manifest themselves not by gross morphological distortions, but by the gradual enlargement of the central galaxy. The simplest way to quantify the sizes of these galaxies is through r_e . In Figure 2 we show the distribution of semi-major axis r_e from the GIM2D pure de Vaucouleurs bulge fits to our BCGs (*black histogram*). To avoid “double-weighting” MS1621 because it is a binary BCG, we only include BCG MS1621a. The choice of BCG in MS1621 is inconsequential for this discussion because both galaxies of the “BCG pair” have similar effective radii. We find that our high redshift BCGs have a biweight-estimated effective

radius of 8.3 ± 1.4 kpc in the NICMOS images. We compare to the local sample of Graham et al. (1996; *shaded histogram*) who fit the surface brightness profiles of BCGs from 119 Abell clusters at $z \leq 0.05$ in the R -band with a standard de Vaucouleurs profile (i.e. $n = 4$) assuming $H_0 = 80 \text{ km s}^{-1} \text{ Mpc}^{-1}$. Their low redshift BCGs have a biweight-estimated effective radius (measured along the semi-major axis as for our sample) of 16.1 ± 1.7 kpc which is ~ 2 times larger than that of our NIC2 high redshift sample. To quantitatively assess the significance of this difference in r_e , we randomly select subsets of 16 BCGs from the Graham et al. (1996) local BCG sample and compute a biweight-estimated r_e for each subset. Using 500 Monte Carlo realizations of the high redshift BCG sample drawn from the low redshift sample, we find that $< 3\%$ (13 of 500) of the realizations have a biweight-estimated r_e less than 8.3 kpc. However, the result is qualitatively different if we use the $F814W$ r_e 's of the 9 BCGs with WFPC2 images. The biweight-estimated r_e for that sample is 18.2 ± 5.1 kpc — larger than, and fully consistent with, the radii of the local sample.

4.3. Are Optical and Infrared Radii Expected to be the Same?

The discrepancy between the results for the NIC2 and WFPC2 radii of our high-redshift BCG sample is either due to systematic errors in the NIC2 measurements or to a real feature of BCGs. If systematic errors are to blame, they would have to be substantially larger than the simulations in Section 3.4 would suggest. Is it possible that effective radii in the rest-frame range 4578–5676 Å ($F814W$ at $z = 0.6$) are systematically different from effective radii measured in the rest-frame range 8750–11250 Å ($F160W$ at $z = 0.6$)? Unfortunately, there are no large local samples of BCGs with both optical and near-infrared photometric parameters. However, a tantalizing hint may come from the E/S0 sample of Pahre (1999). Pahre measured global photometric parameters for a sample of 341 nearby early-type galaxies in the near-infrared K -band. The majority (85%) of the galaxies in the Pahre sample reside in 13 rich clusters with additional galaxies drawn from loose groups (12%) and the field (3%). The K -band sample was complemented with optical V -band data from the literature. In Figure 3 we plot the V -band effective radius versus the K -band effective radius for the 273 galaxies with both measurements. The dashed line is the one-to-one line. It is immediately obvious that the V -band radii are systematically larger than the K -band ones, and the discrepancy increases with increasing radius. At $\log r_e = 1.5$ in K , the V radii are about 1.8 times larger than the K radii. As explained in Pahre et al. (1998), this difference is due to the presence of color gradients. Given that BCGs are a distinct class of objects, it is unclear whether BCG radii could exhibit the same type of wavelength dependence as the E/S0's. However, if they do, then the discrepancy between our NIC2 and WFPC2 radii would be explained, and the actual size evolution of the BCGs between $z = 0$ and 0.6 would be bounded by the WFPC2 images, which are bluer in the rest-frame than the local sample, and the NICMOS images, which are redder in the rest-frame than the local sample.

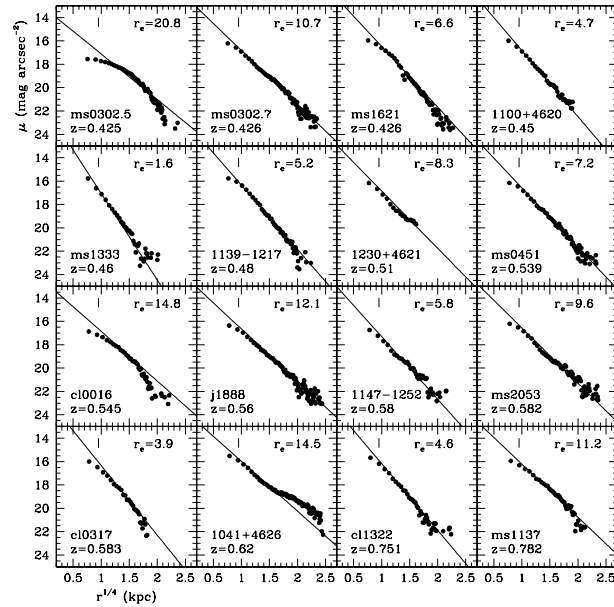


FIG. 1.— The surface brightness profiles of our 16 BCGs ordered by increasing redshift. The filled circles are the data and the line is the best fitting de Vaucouleurs ($r^{1/4}$) profile. The vertical mark in the upper left corner denotes the angular resolution limit (i.e. FWHM of the point spread function) of the NICMOS images. All but three of our BCGs are well described by a de Vaucouleurs profile beyond the resolution limit and out to at least ~ 2 NIC2 r_e . The notable exceptions are MS0302.5+1717, CL0016, and 1041+4626. The BCG MS0302.5+1717 is actually best-fit by a pure exponential disk profile, the BCG CL0016 has a prominent dust lane, and the BCG 1041+4626 lies at the corner of a frame where the local background varies significantly.

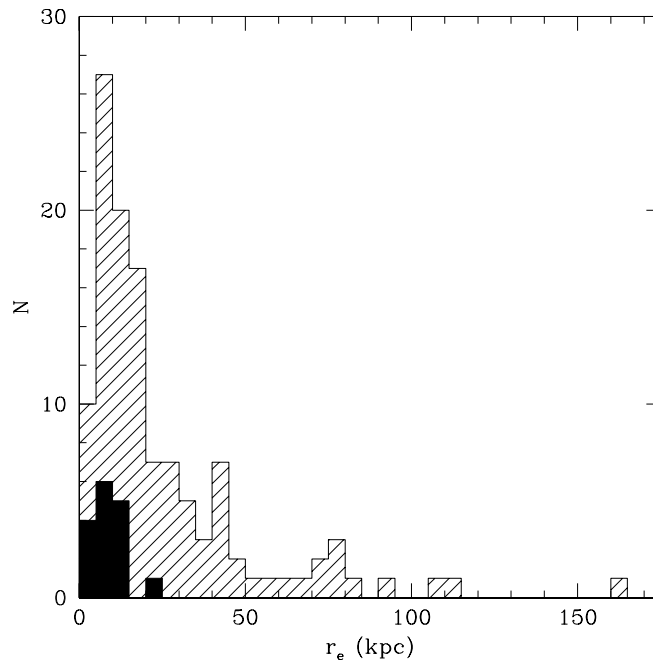


FIG. 2.— The distribution of NIC2 semi-major axis effective radius, r_e , from the GIM2D pure de Vaucouleurs bulge fits to our high-redshift BCG sample (*black histogram*) compared to the local Abell sample of Graham et al. (1996) (*shaded histogram*).

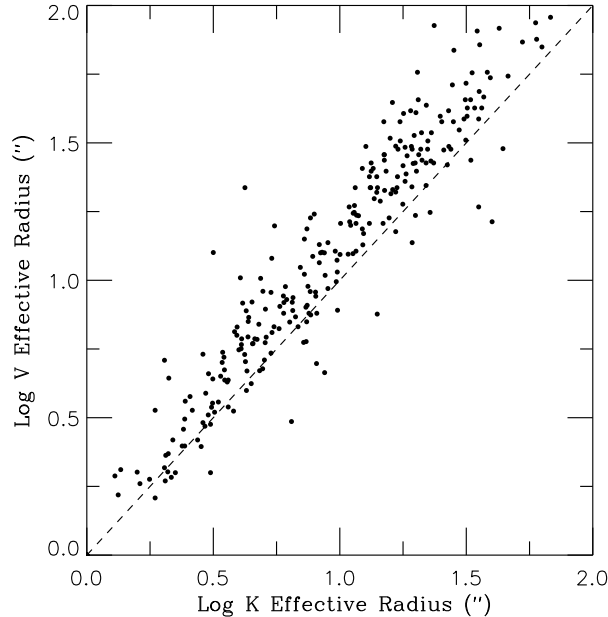


FIG. 3.— Log V effective radius and log K effective radius in arcseconds for 273 E/S0 galaxies from the sample of Pahre (1999). The dashed line is the one-to-one line.

4.4. Accretion Rates

Observations of BCGs show that the relation between $\log \sigma$ and M (i.e., the Faber-Jackson relation; 1976) is rather flat, i.e. BCGs are overluminous for their velocity dispersions (Malumuth & Kirshner 1981, 1985; Oegerle & Hoessel 1991). This result has been interpreted as support for dissipationless merger scenarios for BCGs in which their masses, luminosities, and effective radii increase, but their velocity dispersions remain constant because $\sigma^2 \propto M/R$. Because our high redshift BCGs do not exhibit any signs of recent major interactions, we presume that they are in dynamical equilibrium and that they follow the same scaling relations as local BCGs. Consequently, if their mass scales directly with r_e , we would infer from the comparison of NIC2 and local effective radii that BCGs as a class have doubled in mass since $z \sim 0.5 - 0.6$. Using the semi-analytic model predictions of both the Durham (Cole et al. 1994; Baugh et al. 1996) and Munich (Kauffman et al. 1993) groups, ABK98 present the increase in BCG mass as a function of redshift. For CDM models with $\Omega_m = 1$ our inferred mass accretion rate since $z \sim 0.5$ is in excellent agreement with the model predictions. For low density CDM models with our adopted cosmology ($\Omega_m = 0.2$), they predict slightly less mass accretion by BCGs since $z \sim 0.5$ (a factor of ~ 1.5 increase in mass), but given the large observational uncertainties our findings are still in agreement.

On the other hand, the effective radii from the WFPC2 images show no significant difference from the local BCG sample and would thus be consistent with very little or *no* mass accretion since $z = 0.5 - 0.6$. If this is indeed the case, then we may be faced with the continuing puzzle of a class of galaxies with sizes and magnitudes that show little or no discernible evolution with redshift even though their stellar population must at least be passively evolving (and

are observed to be passively evolving; Nelson et al. 2001b). Part of the possible resolution to this puzzle lies in the fact that evolution is tied to environment. The majority of our BCGs reside in clusters that fall in the high X-ray luminosity category ($L_x > 2.3 \times 10^{44}$ ergs s^{-1}). As noted in the introduction, the luminosities of high L_x BCGs do match the predictions of passive evolution models (Burke et al. 2000; Nelson et al. 2001b), which limits the possible amount of mass these BCGs accrete to less than a factor of 2. Despite their inherent systematic uncertainties, our NIC2/WFPC2 results are sufficient to rule out accretion rates higher than a factor of 2 in high L_x BCGs, but our results cannot be used to place constraints on accretion rates below that level.

We emphasize that our inferred BCG mass accretion rates do not rest on the assumption that the same galaxy identified as the BCG at high redshift remains the BCG to the present day. Indeed the brightest galaxy in any given cluster may very well change over time, but this process is part of the evolution one aims to study. The value of BCGs in evolutionary studies is their relatively unambiguous selection criteria *as a class* in both the data and simulations.

5. SUMMARY

Using high angular resolution F160W NICMOS imaging, we measure the luminosity profiles of 16 BCGs at $0.4 < z < 0.8$. The heterogeneous sample is drawn from existing optical and x-ray surveys published in the literature (Spinrad 1980; Koo 1981; Gunn et al. 1986; Couch et al. 1991; Gioia & Luppino 1994; Gonzalez et al. 2001). Archival WFPC2 F814W images were also available for 9 of the 16 BCGs. Our primary conclusions are that: 1) the NICMOS surface brightness profiles of high redshift BCGs are well described by a de Vaucouleurs profile ($r^{1/4}$) out to a radius of at least ~ 2 NIC2 r_e ,

2) the NICMOS effective radii of our high redshift BCGs are, on average, ~ 2 times smaller than those of local samples (Graham et al. 1996) for $H_0 = 80 \text{ km s}^{-1} \text{ Mpc}^{-1}$, $\Omega_m = 0.2$, and $\Omega_\Lambda = 0.0$. Using simple dynamical equilibrium arguments, this result suggests that BCGs have increased in mass by a factor of ~ 2 since $z \sim 0.5$.

3) the WFPC2 effective radii are fully consistent with those of the local sample, which would suggest little or no mass accretion. The discrepancy between the NICMOS and WFPC2 results is either due to systematic errors in the NICMOS measurements or to a real physical property of BCGs such as color gradients. If systematic errors are to blame, they would have to be substantially larger than the $\sim 20\%$ systematic radius error suggested by our simulations. Supporting our suggestion that this difference is not due to a systematic error, we note that the optical effective radii of local E/S0 galaxies are larger than their near-infrared values due to color gradients. If the effective radii of BCGs exhibit a similar wavelength dependence, it would reconcile our NICMOS and WFPC2 radii. Given that our WFPC2 and NICMOS data are both bluer and redder in the rest-frame than the R-band local sample, the results from the two data sets bound the possible evolution of r_e , and hence the accretion.

Although this sample marks a significant improvement in the quality of data available for high redshift BCGs, our sample is too small to fully resolve systematic uncertainties and to confidently constrain mass accretion rates below a factor of 2. However, our work demonstrates the feasi-

bility of using high resolution imaging to measure BCG structural parameters at $z > 0.5$. With a sufficiently large sample, complemented with some velocity dispersion measurements to determine whether the scaling relations hold, such an approach has the potential to definitively address the issue of mass accretion by BCGs since $z \sim 1$.

Acknowledgments: AEN would like to thank Kim-Vy Tran (and her GIM2D Cookbook) for her help in understanding the intricacies of GIM2D. AEN and AHG acknowledge funding from a NSF grant (AST-9733111). AEN gratefully acknowledges financial support from the University of California Graduate Research Mentorship Fellowship program. AHG acknowledges funding from the ARCS Foundation and the CfA postdoctoral fellowship program. DZ acknowledges financial support from a NSF CAREER grant (AST-9733111), a David and Lucile Packard Foundation Fellowship, and an Alfred P. Sloan Fellowship. This work was partially supported by NASA through grant number GO-07327.01-96A from the Space Telescope Science Institute, which is operated by the Association of Universities for Research in Astronomy, Inc., under NASA contract NAS5-26555.

REFERENCES

- Aragon-Salamanca, A., Baugh, C.M., & Kauffmann, G. 1998, *MNRAS*, 297, 427 (ABK98)
- Aragon-Salamanca, A., Ellis, R.S., Couch, W.J., & Carter, D. 1993, *MNRAS*, 262, 764
- Baugh, C.M., Cole, S., & Frenk, C.S. 1996, *MNRAS*, 283, 1361
- Bertin, E., & Arnouts, S. 1996, *A&AS*, 117, 393
- Burke, D.J., Collins, C.A., & Mann, R.G. 2000, *ApJ*, 532, 105L
- Carter, D. 1985, in *New Aspects of Galaxy Photometry: Proceedings of the Specialized Meeting*, (Berlin and New York: Springer-Verlag), 215
- Clowe, D.I. 1998, *ApJ*, 497, L61
- Clowe, D.I., Luppino, G.A., Kaiser, N., & Gioia, I.M. 2000, *ApJ*, 539, 540
- Cole, S., Aragon-Salamanca, A., Frenk, C.S., Navarro, J.F., Zepf, S.E. 1994, *MNRAS*, 271, 781
- Couch, W.J., Ellis, R.S., MacLaren, I., & Malin, D.F. 1991, *MNRAS*, 249, 606
- Dalcanton, J.J., Spergel, D.N., Gunn, J.E., Schmidt, M., & Schneider, D.P. 1997, *AJ*, 118, 719
- Dressler, A. 1978, *ApJ*, 223, 765
- Dressler, A. 1979, *ApJ*, 231, 659
- Dressler, A. 1987, in *Nearly Normal Galaxies From the Planck Time to the Present: Proceedings of the Eighth Santa Cruz Summer Workshop*, (New York: Springer-Verlag), 276
- Faber, S.M., & Jackson, R.E. 1976, *ApJ*, 204, 668
- Fisher, D., Illingworth, G., & Franx, M. 1995, *ApJ*, 438, 539
- Gioia, I.M. & Luppino, G.A. 1994, *ApJS*, 94, 583
- Gonzalez, A.H., Zaritsky, D., Dalcanton, J.J., & Nelson, A.E. 2001, *ApJS*, accepted.
- Graham, A., Lauer, T.R., Colless, M., & Postman, M. 1996, *ApJ*, 465, 534
- Gunn, J.E., Hoessel, J.G., & Oke, J.B. 1986, *ApJ*, 306, 30
- Hoessel, J.G., Gunn, J.E., & Thuan, T.X. 1980, *ApJ*, 241, 486
- Hoessel, J.G., Oegerle, W.R., & Schneider, D.P. 1987, 94, 1111
- Kauffman, G., White, S.D.M., & Guiderdoni, B. 1993, *MNRAS*, 264, 201
- Kelson, D.D., van Dokkum, P., Franx, M., Illingworth, G.D., & Fabricant, D. 1997, *ApJ*, 478, L13
- Koo, D.C. 1981, *ApJ*, 251, L75
- Krist, J. 1993, in *ASP Conf. Ser. 52, Astronomical Data Analysis Software and Systems II*, ed. R. J. Hanisch, R. J. V. Brissenden, and J. Barnes, 536.
- Luppino, G.A., & Gioia, I.M. 1992, *A&A*, 265, 9
- Luppino, G.A., & Gioia, I.M. 1999, *A&A*, 136, 117
- Malumuth, E.M., & Kirshner, R.P. 1981, *ApJ*, 251, 508
- Malumuth, E.M., & Kirshner, R.P. 1985, *ApJ*, 291, 8
- Nelson, A.E., Gonzalez, A.H., Zaritsky, D., & Dalcanton, J.J. 2001a, *ApJ*, in press
- Nelson, A.E., Gonzalez, A.H., Zaritsky, D., & Dalcanton, J.J. 2001b, *ApJ*, submitted
- Oegerle, W.R., & Hoessel, J.G. 1991, *ApJ*, 375, 15
- Oke, J.B., & Gunn, J.E. 1983, *ApJ*, 266, 713
- Ostriker, J.P., & Hausmann, M.A. 1977, *ApJ*, 217, 125L
- Ostriker, J.P., & Tremaine, S.D. 1975, *ApJ*, 202, 113L
- Pahre, M. A., de Carvalho, R. R., & Djorgovski, S. G. 1998, *AJ*, 116, 1606
- Pahre, M. A. 1999, *ApJS*, 124, 127
- Postman, M. & Lauer, T.R. 1995, *ApJ*, 440, 28
- Richstone, D.O. 1976, *ApJ*, 204, 642
- Sandage, A. & Hardy, E. 1973, *ApJ*, 183, 743
- Schlegel, D.J., Finkbeiner, D.P., & Davis, M. 1998, *ApJ*, 500, 525
- Schneider, D.P., Gunn, J.E., & Hoessel, J.G. 1983, *ApJ*, 264, 337
- Schombert, J.M. 1986, *ApJS*, 60, 603
- Sérsic, J.L. 1968, *Atlas de Galaxias Australes* (Cordoba: Observatorio Astronomico)
- Simard, L. 1998, in *A.S.P. Conference Series Vol. 145, Astronomical Data Analysis Software Systems VII*, eds. R. Albrecht, R.N. Hook, & H.A. Bushouse, 108
- Simard, L. et al. 2001, in prep
- Spinrad, H. 1980, in *Proc. IAU Symp. 124, Objects of High Redshift*, eds. G.O. Abell and P.J.E. Peebles, (Dordrecht, D. Reidel Publishing Co.), p. 39.

TABLE 1
HST NICMOS AND WFPC2 BCG IMAGE DATASETS

Cluster ID	α (J2000.0)	δ (J2000.0)	Total Integration Time (s)		CADC Association Dataset ID	
			F160W (4)	F814W (5)	F160W (6)	F814W (7)
CL0016+16	00:18:33.64	+16:26:15.13	768	8400	N42B38010	U2C40101A
J1888.16CL	00:56:56.78	-27:40:31.26	768	8400	N42B39010	U2C40501A
MS0302.5+1717	03:05:18.19	+17:28:23.35	768	...	N42B48010	...
MS0302.7+1658	03:05:31.71	+17:10:02.64	768	2400	N42B49010	U2UL0103A
CL0317+1521 ^a	03:20:01.52	+15:31:57.65	256	2500	N42B40010	U58J0101A
MS0451.6-0305	04:54:10.83	-03:00:56.87	768	10400	N42B50010	U3060101A
1041+4626	10:41:03.81	+46:26:36.24	1056	...	N42B05010	...
1100+4620	11:00:57.40	+46:20:37.88	768	...	N42B15010	...
1139-1217	11:39:57.00	-12:17:19.00	768	...	N42B12010	...
MS1137.5+6625	11:40:23.86	+66:08:18.47	1056	14400	N42B52010	U3060301A
1147-1252	11:47:17.30	-12:52:09.00	768	...	N42B27010	...
1230+4621 ^b	12:30:16.26	+46:21:17.27	512	...	N42B07010	...
CL1322+3027	13:24:48.83	+30:11:38.16	1056	14000	N42B43010	U2840501A
MS1333.3+1725	13:35:47.14	+17:09:39.20	768	...	N42B53010	...
MS1621.5+2640	16:23:35.48	+26:34:12.82	768	4600	N42B55010	U53B0701A
MS2053.7-0449	20:56:21.78	-04:37:50.88	768	3200	N42B56010	U4F30601A

^aTwo of the three dithered exposures for this object had pointing errors

^bOne of the three dithered exposures for this object was lost due to data corruption.

TABLE 2
NIC2/F160W BCG SIZE MEASUREMENTS

BCG	z	Curve Of Growth r_e		Pure Bulge r_e				Bulge+Disk r_{hl}				Better Model
		"	kpc	"	sma	"	circ	"	sma	"	circ	
(1)	(2)	(3)	(4)	(5)	(6)	(7)	(8)	(9)	(10)	(11)	(12)	(13)
CL0016	0.545	0.88	4.50	2.90	14.82	2.09	10.69	1.23	6.29	0.89	4.55	BD
		1.21	6.19									
		1.15	5.88									
J1888	0.560	1.56	8.08	2.34	12.12	2.03	10.51	3.08	15.95	2.93	15.17	EQ
		1.89	9.79									
		1.53	7.92									
MS0302.5	0.425	1.30	5.85	4.61	20.75	3.82	17.19	1.99	8.96	1.65	7.43	BD
		1.62	7.29									
		1.51	6.80									
MS0302.7	0.426	1.51	6.80	2.38	10.72	2.09	9.42	1.61	7.26	1.41	6.35	PB
		1.45	6.53									
		1.36	6.13									
CL0317	0.583	0.38	2.00	0.73	3.85	0.60	3.16	0.51	2.69	0.42	2.22	BD
MS0451	0.539	0.93	4.73	1.41	7.17	1.06	5.39	1.10	5.59	0.82	4.17	PB
		0.85	4.32									
		0.73	3.71									
1041+4626	0.620	2.96	16.04	2.67	14.47	2.40	13.01	2.68	14.53	2.36	12.79	BD
		3.74	20.27									
		3.91	21.19									
1100+4620	0.450	1.00	4.64	1.02	4.73	1.00	4.64	1.23	5.71	1.21	5.62	EQ
		0.91	4.22									
		0.70	3.25									
1139–1217	0.480	0.76	3.65	1.09	5.23	1.04	4.99	1.04	4.99	0.99	4.75	BD
		0.67	3.22									
		0.71	3.41									
MS1137	0.782	1.77	10.51	1.89	11.21	1.84	10.92	1.91	11.34	1.86	11.04	EQ
		1.04	6.17									
		1.08	6.41									
1147–1252	0.580	0.80	4.21	1.11	5.84	0.98	5.16	0.91	4.79	0.82	4.32	EQ
		0.78	4.10									
		0.93	4.89									
1230+4621 ^a	0.510	2.00	9.90	1.68	8.32	1.58	7.82	1.96	9.70	1.72	8.52	BD
		1.62	8.02									
CL1322	0.751	0.61	3.57	0.78	4.56	0.57	3.34	0.76	4.45	0.55	3.22	EQ
		0.95	5.56									
		0.54	3.16									
MS1333	0.460	0.50	2.35	0.33	1.55	0.33	1.55	0.47	2.21	0.47	2.21	BD
		0.58	2.72									
		0.54	2.54									
MS1621a	0.426	0.88	3.97	1.46	6.58	1.28	5.77	1.05	4.73	0.99	4.46	PB
		0.76	3.42									
		0.80	3.60									
MS1621b	0.426	0.81	3.65	1.36	6.13	1.33	5.99	1.09	4.91	0.90	4.06	BD
		0.75	3.38									
		0.88	3.96									
MS2053	0.582	1.46	7.70	1.82	9.59	1.75	9.22	1.77	9.33	1.71	9.01	PB
		1.43	7.54									
		1.17	6.17									

^aOne of the three dithered exposures for this object was lost due to data corruption.

TABLE 3
WFPC2/F814W BCG SIZE MEASUREMENTS

BCG	Curve Of Growth r_e		Pure Bulge r_e				Bulge+Disk r_{hl}				Pure Sérsic r_e				Sérsic Index n
	"	kpc	sma	circ	sma	circ	sma	circ	sma	circ	sma	circ			
(1)	(2)	(3)	(4)	(5)	(6)	(7)	(8)	(9)	(10)	(11)	(12)	(13)	(14)	(15)	(16)
CL0016	3.20	16.36	<u>8.50</u>	43.46	6.96	35.59	5.67	28.99	4.96	25.36	6.04	30.88	4.98	25.46	3.3
			8.98	45.91	7.35	37.58	5.02	25.67	4.39	22.44	6.46	33.02	5.29	27.05	3.4
J1888	2.76	14.29	4.43	22.94	4.01	20.77	<u>3.27</u>	16.93	3.14	16.26	6.66	34.49	6.03	31.23	4.9
			4.26	22.06	3.86	19.99	2.48	12.84	2.38	12.32	6.60	34.18	5.98	30.97	4.9
MS0302.7	2.76	12.44	4.77	21.49	4.22	19.01	3.30	14.87	<u>2.69</u>	12.12	5.34	24.06	4.72	21.27	4.3
			5.08	22.89	4.50	20.28	3.28	14.78	2.68	12.08	7.02	31.63	6.24	28.12	4.7
CL0317	0.53	2.80	0.91	4.80	0.66	3.48	0.60	3.16	0.51	2.69	0.60	3.16	0.44	2.32	2.5
			0.93	4.91	0.67	3.53	<u>0.58</u>	3.06	0.50	2.64	0.59	3.11	0.43	2.27	2.4
MS0451	2.87	14.60	4.19	21.31	3.54	18.00	<u>3.75</u>	19.07	2.33	11.85	6.79	34.53	5.76	29.29	5.1
			3.85	19.58	3.27	16.63	3.68	18.72	2.29	11.65	6.14	31.23	5.21	26.50	4.9
MS1137	2.83	16.80	4.49	26.52	4.31	25.58	3.53	20.95	3.02	17.93	5.51	32.71	5.28	31.34	4.5
			4.56	27.07	4.56	27.07	<u>3.57</u>	21.19	3.06	18.16	4.95	29.38	4.75	28.20	4.3
CL1322	1.17	6.85	<u>1.15</u>	6.73	1.08	6.32	2.36	13.81	2.31	13.52	1.95	11.41	1.83	10.71	5.4
			1.08	6.32	1.02	5.97	1.10	6.44	1.08	6.32	1.95	11.41	1.83	10.71	5.4
MS1621a	...		2.66	11.99	2.51	11.31	3.65	16.45	3.15	14.19	3.25	14.64	3.05	13.74	4.8
			1.96	8.83	1.84	8.29	<u>2.01</u>	9.06	1.73	7.80	1.44	6.49	1.34	6.04	3.2
MS1621b	...		2.07	9.33	2.03	9.15	<u>2.24</u>	10.09	1.58	7.12	1.68	7.57	1.65	7.43	3.4
			1.96	8.83	1.93	8.70	1.74	7.84	1.23	5.54	1.05	4.73	1.02	4.60	2.5
MS2053	1.77	9.33	<u>2.32</u>	12.23	2.05	10.81	2.33	12.28	2.02	10.65	2.19	11.54	1.92	10.12	3.8
			2.28	12.02	2.00	10.54	1.52	8.01	1.32	6.96	1.93	10.17	1.69	8.91	3.6

TABLE 4
WFPC2 BCG ISOPHOTAL ELLIPSE FITTING

BCG	Fitting Range in $r^{1/4}$	r_e sma	Δe (ISO)	Δe (GIM2D)	$\Delta\phi$ (ISO)	$\Delta\phi$ (GIM2D)	Δx pixels	Δy pixels
(1)	(2)	(3)	(4)	(5)	(6)	(7)	(8)	(9)
CL0016	1.1 – 2.8	8.35	+0.14	+0.19	-23	-31	+3	-2
J1888	1.0 – 2.1	5.71	+0.10	0.00	-25	-30	0	0
MS0302.7	1.1 – 3.0	7.02	+0.15	+0.39	+20	+10	0	-3
CL0317	1.5 – 2.3	0.28	+0.10	+0.25	0	+ 2	0	+2
MS1137	1.1 – 2.6	6.32	+0.14	+0.26	-30	-47	0	0
CL1322	1.1 – 2.3	1.31	-0.05	0.00	-20	+20	+2	+2
MS2053	1.3 – 2.6	2.35	-0.10	-0.20	+24	+60	0	0

TABLE 5
NIC2 BCG SIZE MEASUREMENT SIMULATIONS

BCG	Model Type	Input r_{hl} sma	Input r_{hl} circ	Recovered COG r_{hl}	F_r	F_f
(1)	(2)	(3)	(4)	(5)	(6)	(7)
CL0016	NIC2 $r^{1/4}$	2.89	2.26	0.95	0.42	0.51
	NIC2 B+D	1.28	0.92	1.02	1.10	0.89
	WFPC2 $r^{1/4}$	4.86	3.80	1.12	0.30	0.38
MS0302.7	NIC2 $r^{1/4}$	2.38	2.26	1.73	0.77	0.82
	NIC2 B+D	1.61	1.42	1.72	1.21	1.07
	WFPC2 $r^{1/4}$	3.46	3.28	3.97	1.21	1.16
MS1137	NIC2 $r^{1/4}$	1.89	1.81	1.53	0.85	0.88
	NIC2 B+D	1.92	1.86	1.56	0.84	0.89
	WFPC2 $r^{1/4}$	3.72	3.55	2.90	0.82	0.95
CL1322	NIC2 $r^{1/4}$	0.78	0.57	0.46	0.81	0.66
	NIC2 B+D	0.76	0.55	0.42	0.77	0.63
	WFPC2 $r^{1/4}$	2.70	1.97	0.61	0.31	0.28
MS2053	NIC2 $r^{1/4}$	1.82	1.62	1.42	0.88	0.98
	NIC2 B+D	1.77	1.70	1.61	0.94	1.04
	WFPC2 $r^{1/4}$	2.52	2.24	1.68	0.75	0.90